Resonating quantum three-coloring wave functions for the kagome quantum antiferromagnet

Hitesh J. Changlani, Sumiran Pujari, Chia-Min Chung, and Bryan K. Clark

Phys. Rev. B **99**, 104433 — Published 27 March 2019

DOI: 10.1103/PhysRevB.99.104433

Resonating quantum three-coloring wavefunctions for the kagome quantum antiferromagnet

Hitesh J. Changlani,[1,2] Sumiran Pujari,[3] Chia-Min Chung,[4] and Bryan K. Clark[5]

[1]*Department of Physics, Florida State University, Tallahassee, Florida 32306, USA*
[2]*Department of Physics and Astronomy, Johns Hopkins University, Baltimore, MD 21218 and Institute for Quantum Matter, Johns Hopkins University, Baltimore, MD 21218*
[3]*Department of Physics, Indian Institute of Technology Bombay, Mumbai, MH 400076, India*
[4]*Department of Physics and Arnold Sommerfeld Center for Theoretical Physics, Ludwig-Maximilians-Universitat Munchen, Theresienstrasse 37, 80333 Munchen, Germany*
[5]*Institute for Condensed Matter Theory and Department of Physics, University of Illinois at Urbana-Champaign, USA*

(Dated: January 7, 2019)

Motivated by the recent discovery of a macroscopically degenerate exactly solvable point of the spin-$1/2$ XXZ model for $J_z/J = -1/2$ on the kagome lattice [H. J. Changlani et al. Phys. Rev. Lett 120, 117202 (2018)] – a result that holds for arbitrary magnetization – we develop an exact mapping between its exact "quantum three-coloring" wavefunctions and the characteristic localized and topological magnons. This map, involving "resonating two-color loops", is developed to represent exact many-body ground state wavefunctions for special high magnetizations. Using this map we show that these exact ground state solutions are valid for any $J_z/J \geq -1/2$. This demonstrates the equivalence of the ground-state wavefunction of the Ising, Heisenberg and XY regimes all the way to the $J_z/J = -1/2$ point for these high magnetization sectors. In the hardcore bosonic language, this means that a certain class of exact many-body solutions, previously argued to hold for purely *repulsive* interactions ($J_z \geq 0$), actually hold for *attractive* interactions as well, up to a critical interaction strength.

For the case of zero magnetization, where the ground state is not exactly known, we perform density matrix renormalization group calculations. Based on the calculation of the ground state energy and measurement of order parameters, we provide evidence for a lack of any qualitative change in the ground state on finite clusters in the Ising ($J_z \gg J$), Heisenberg ($J_z = J$) and XY ($J_z = 0$) regimes, continuing adiabatically to the vicinity of the macroscopically degenerate $J_z/J = -1/2$ point. These findings offer a framework for recent results in the literature, and also suggest that the $J_z/J = -1/2$ point is an unconventional quantum critical point whose vicinity may contain the key to resolving the spin-$1/2$ kagome problem.

I. INTRODUCTION

Quantum frustrated magnetism presents one of the most intriguing and intricate examples of the interplay between spatial geometry and quantum mechanics. This results in a rich multitude of competing exotic phases such as valence bond solids, topological phases including several spin liquids, and magnetically ordered phases. Slight changes in the material composition or geometry can lead to a dramatic change in its phase, making frustrated magnets ideal playgrounds to study quantum phase transitions.

The building blocks of many of these systems are lattices of magnetic ions made from motifs of connected triangles. Prominent amongst these is the kagome lattice, a lattice of corner sharing triangles which has been intensely studied owing to its relevance to materials such as Herbertsmithite (a kagome lattice of Cu^{2+} ions)[1]. Experiments on Herbertsmithite[2,3]– of which the idealized kagome Heisenberg antiferromagnet is known to be a good model[4] – find that spins do not order even at the lowest investigated temperatures (50 mK, a small fraction of the exchange energy of $\sim$ 200 K), tantalizingly suggesting the picture of a two-dimensional spin-liquid ground state. However, in spite of several theoretical efforts devoted to the idealized model, there is no universal consensus on the precise nature of the spin liquid ground state[5–15] and recent work even suggests that larger lattices should stabilize an ordered state[16]. To reconcile some of these observations, it has been suggested that the kagome Heisenberg model lies at or close to a critical point in the phase diagram in a suitably chosen parameter space of model Hamiltonians[17,18].

Previous work (by two of us, HJC and BKC in collaboration with others) contributed to the understanding of the kagome phase diagram through the discovery of an extensively *quantum* degenerate exactly solvable point[17]. While the *classical* extensive degeneracy for the kagome and hyper-kagome lattice has a long history, the connection to the quantum case in the spin-1/2 XXZ Hamiltonian,

$$H_{XXZ}[J_z] = J \sum_{\langle i,j \rangle} S_i^x S_j^x + S_i^y S_j^y + J_z \sum_{\langle i,j \rangle} S_i^z S_j^z \qquad (1)$$

at $H_{\mathrm{XXZ}}[J_z = -1/2, J = 1]$ (notated as H_{XXZ0}[19]), has not been entirely explored. S_i are spin-1/2 operators on site i, $\langle i,j \rangle$ refer to nearest neighbor pairs and J (set to 1 throughout the paper) and J_z are the XY and Ising couplings respectively. Ref.[17] showed that the quantum degeneracy exists in *all* S_z sectors and all finite (or infinite) system sizes. Numerical investigations on the highly symmetric $36d$ cluster[20] showed how the $XXZ0$ point on the kagome lattice is embedded in the wider phase diagram. We note that Ref.[21] studied the phase diagram of the triangular lattice in the vicinity of $J_z = -1/2$.

At $J_z = -1/2$, the exact solutions apply to any lattice of triangular motifs with the Hamiltonian of the form,

$$H = \sum_{\triangle} H_{XXZ0}(\triangle) \qquad (2)$$

where $H_{XXZ0}(\triangle)$ is the $XXZ0$ Hamiltonian on a single tri-

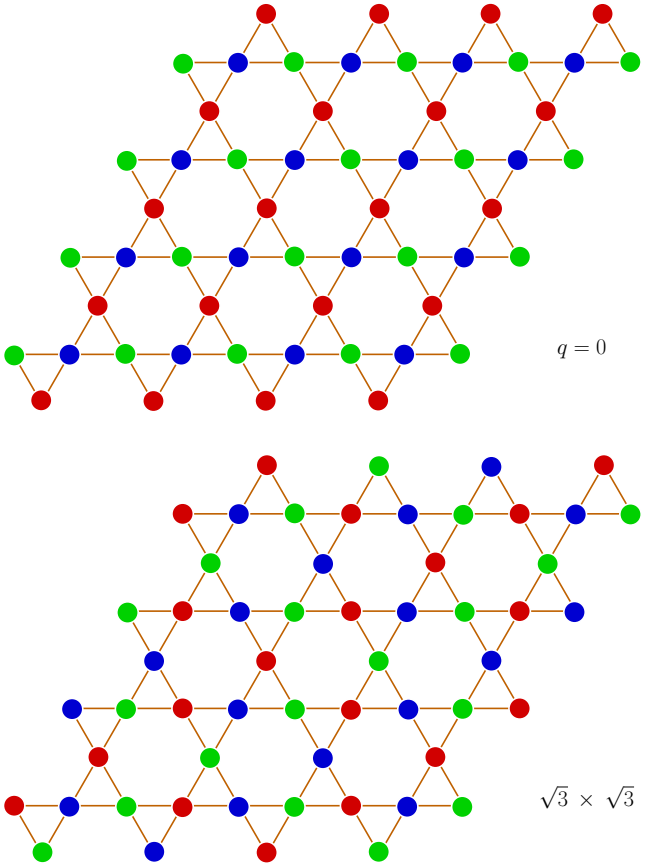

Figure 1. (Color online) Two representative three-colorings on the kagome lattice corresponding to the $q = 0$ and $\sqrt{3} \times \sqrt{3}$ solutions. The colors red, blue and green represent the classical 120° states or their quantum equivalents.

angle $\triangle$ as long as the vertices are consistently colorable by three colors such that no two vertices connected by a bond have the same color. For the kagome lattice, we show representative three-colorings in Fig. 1 which depict the so-called $q = 0$ and $\sqrt{3} \times \sqrt{3}$ patterns[22]. (Other three-colorable lattices include the triangular lattice, the Shastry-Sutherland lattice, the hyperkagome lattice, the squagome lattice and the icosidodecahedron.)

In this work, we employ the quantum three-colorings as a means of gaining analytic intuition for the physics near the highly degenerate $J_z = -1/2$ point. Our work will highlight the relevance of this point in controlling the physics seen in the Heisenberg regime i.e. $J_z = 1$. For this purpose, we decompose the XXZ Hamiltonian (1) as,

$$H_{XXZ}[J_z] = H_{XXZ0} + \left(J_z + \frac{1}{2}\right) \sum_{\langle i,j \rangle} S_i^z S_j^z \tag{3}$$

$$= H_{XXZ0} + \left(J_z + \frac{1}{2}\right) H_{zz} \tag{4}$$

and ask if it is possible to simultaneously minimize both parts of the Hamiltonian. While this is not possible in the most general circumstances, we find that at high magnetization (equivalently, low fillings in the hardcore bosonic language) the Hamiltonian is "frustration free" i.e. it is *indeed* possible to achieve this minimization.

Since the map between spin 1/2 and hardcore bosons is used often in the paper, we clarify the terminology associated with it. Down spins in a background of up spins are equivalent to hardcore bosons in a vacuum and thus we interchangeably use the words "filling" and "magnetization" in the course of our discussions. More precisely, the spin (S_i) and hardcore boson operators (b_i) are related as,

$$b_i^\dagger = S_i^+ \quad b_i = S_i^- \quad n_i = b_i^\dagger b_i = \frac{1}{2} - S_i^z \tag{5}$$

and thus the XXZ Hamiltonian reads,

$$H_{XXZ}(J_z) = \frac{1}{2} \sum_{\langle i,j \rangle} b_i^\dagger b_j + \text{h.c.} + J_z \sum_{\langle i,j \rangle} n_i n_j + d \tag{6}$$

where d is a constant in a given magnetization sector that equals $J_z \left(\frac{N}{2} - 2\sum_i n_i\right)$ for a N site kagome lattice. We also use the term "magnon" to denote the wavefunction of one down spin in a sea of up spins, or equivalently the wavefunction of a single hardcore boson in vacuum.

The remainder of the paper is organized as follows. In Sec. II, we recapitulate the nature of the exact (ground state) solutions for $J_z = -1/2$ and why they exist in every magnetization sector. For this we define quantum three-colors, the quantum version of the 120° classical ground states, which provides a convenient choice of variables for explaining several of our numerical observations. In Sec. III, we develop the concept of resonating color loops (RCL) which is the basis of an exact mapping relating the coloring wavefunctions to magnons. We discuss in detail the crucial effects due to S_z (or number) projection. Using the RCL construct, in Sec. IV, we revisit the more familiar localized and topological magnon modes, which arise from the flatband that exists on the kagome lattice. We show that each such mode has a direct connection to a RCL. In Sec. V these ideas are further extended to express exact many body ground state wavefunctions for special high magnetizations as projected quantum three-coloring wavefunctions. We find that for these special magnetization sectors, the exact ground state, a quantum three-coloring superposition, holds for all $J_z \geq -1/2$ which shows the equivalence of the Ising, Heisenberg and XY regimes.

For the case of zero magnetization, we have investigated the relevance of the $J_z = -1/2$ point (and hence the three-coloring manifold) by performing large scale density matrix renormalization group (DMRG) calculations for a large range of J_z in Sec. VI. These results extend the results of previous exact diagonalizations[17] to bigger systems which support H_{XXZ0} being a quantum critical point in the XXZ phase diagram. In Sec. VII, we conclude by summarizing our results and suggesting future avenues for further exploration.

II. QUANTUM THREE-COLORS AND THE EXACT SOLUTION OF H_{XXZ0}

We state the central result of Ref.[17], where it was proved that any Hamiltonian of the form of Eq. (2) for $J_z = -1/2$, has ground states of the form,

$$|C\rangle \equiv P_{S_z}\Big(\prod_{\text{valid}} \otimes |\gamma_s\rangle\Big) \tag{7}$$

where $\{|\gamma_s\rangle = |r\rangle, |b\rangle \text{ or } |g\rangle\}$, denoted as colors on site s are defined as,

$$\begin{aligned} |r\rangle &\equiv \frac{1}{\sqrt{2}}\Big(|\uparrow\rangle + |\downarrow\rangle\Big) \\ |b\rangle &\equiv \frac{1}{\sqrt{2}}\Big(|\uparrow\rangle + \omega|\downarrow\rangle\Big) \\ |g\rangle &\equiv \frac{1}{\sqrt{2}}\Big(|\uparrow\rangle + \omega^2|\downarrow\rangle\Big) \end{aligned} \tag{8}$$

where $\omega = e^{i2\pi/3}$. Taking the quantization axis to be the z-axis, the colors correspond to spin directions in the xy plane that are at 120° relative to one another. Valid colorings satisfy the three-coloring condition i.e. exactly one $|r\rangle$, one $|b\rangle$ and one $|g\rangle$ per triangular motif. These are depicted by colors red, blue and green respectively in our figures. P_{S_z} projects into a particular total S_z sector.

The construction (7) is referred to as the three-coloring condition and any such many body state which satisfies the constraint conditions is a three-coloring state. Such states have primarily been studied in the context of the classical kagome antiferromagnet at the Heisenberg point[19,22–29].

Classically, a Luttinger-Tisza analysis[30] of H_{XXZ} shows that $J_z = -1/2$ is a critical point in the kagome phase diagram. To see this, we recast Eq. (1) in reciprocal space,

$$\sum_{\mathbf{q}} \Big(\tilde{\mathbf{S}}_{XY}(\mathbf{q})^T \cdot \Big[\tilde{J}(\mathbf{q})\Big] \cdot \tilde{\mathbf{S}}_{XY}(-\mathbf{q}) + J_z\, \tilde{\mathbf{S}}_Z(\mathbf{q})^T \cdot \Big[\tilde{J}(\mathbf{q})\Big] \cdot \tilde{\mathbf{S}}_Z(-\mathbf{q}) \Big) \tag{9}$$

where,

$$\tilde{\mathbf{S}}_{XY}(\mathbf{q}) = \frac{1}{\sqrt{N_u}} \sum_{\mathbf{r}} e^{-i\mathbf{q}\cdot\mathbf{r}} \begin{pmatrix} \mathbf{S}^{XY}_{\mathbf{r},1} & \mathbf{S}^{XY}_{\mathbf{r},2} & \mathbf{S}^{XY}_{\mathbf{r},3} \end{pmatrix}^T \tag{10}$$

$$\tilde{\mathbf{S}}_{Z}(\mathbf{q}) = \frac{1}{\sqrt{N_u}} \sum_{\mathbf{r}} e^{-i\mathbf{q}\cdot\mathbf{r}} \begin{pmatrix} \mathbf{S}^{z}_{\mathbf{r},1} & \mathbf{S}^{z}_{\mathbf{r},2} & \mathbf{S}^{z}_{\mathbf{r},3} \end{pmatrix}^T \tag{11}$$

$$\Big[\tilde{J}(\mathbf{q})\Big] = \frac{1}{2} \begin{pmatrix} 0 & 1+e^{i\mathbf{q}\cdot\mathbf{a_2}} & 1+e^{i\mathbf{q}\cdot(\mathbf{a_2}-\mathbf{a_1})} \\ 1+e^{-i\mathbf{q}\cdot\mathbf{a_2}} & 0 & 1+e^{-i\mathbf{q}\cdot\mathbf{a_1}} \\ 1+e^{-i\mathbf{q}\cdot(\mathbf{a_2}-\mathbf{a_1})} & 1+e^{i\mathbf{q}\cdot\mathbf{a_1}} & 0 \end{pmatrix} \tag{12}$$

$\mathbf{a_1}$, $\mathbf{a_2}$ are the primitive lattice vectors (considering one up-triangle with three sites as the Kagome unit cell), and $\mathbf{q}$ is restricted to the first Brillouin zone and N_u is the number of unit cells. $\mathbf{S}_{\mathbf{r},\mu}$ is a classical spin of unit magnitude at site $\mathbf{r}, \mu$, where r labels the unit cell and μ labels the site within the unit cell. $\mathbf{S}^{XY}_{\mathbf{r},\mu}$ and $\mathbf{S}^{Z}_{\mathbf{r},\mu}$ are the projections of the unit vector $\mathbf{S}_{\mathbf{r},\mu}$ on to the xy plane and z axis respectively.

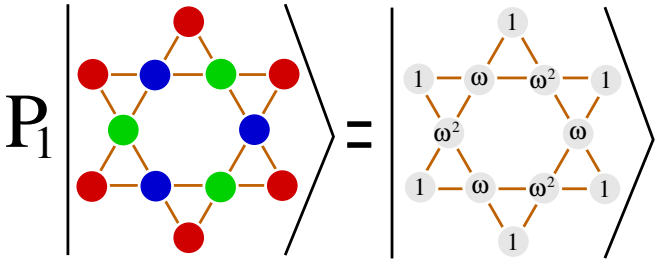

Figure 2. (Color online) Representative example of a single magnon state with amplitudes $1, \omega, \omega^2$ in the three-coloring basis, written as a many-body coloring wavefunction with a projection operator.

For the classical ground state, the two terms in Eq. (9) are competing. For $J_z < -1/2$, the second term in Eq. (9) wins giving a unique ferromagnetic ground state at $\mathbf{q} = 0$ with all spins pointing in the z direction. For $J_z > -1/2$, the first term in Eq. (9) wins, giving a flat-band solution with all $\mathbf{q}$ being classically degenerate to each other in energy, with the spins oriented in the xy plane. They give rise to an extensively degenerate ground state manifold since there are infinite ways in which these classically degenerate solutions at different $\mathbf{q}$ may be linearly combined while respecting the Luttinger-Tisza condition $\sum_{\mathbf{q}} \tilde{\mathbf{S}}_{XY}(\mathbf{q}) \cdot \tilde{\mathbf{S}}_{XY}(-\mathbf{q}) = 1$. At the Heisenberg point, this extensively degenerate classical ground state manifold has also been noted in the literature before[31–33].

Since the classical spins lie in the xy plane for $J_z > -1/2$, they are impervious to the J_z term. Any state that then locally satisfies the three-coloring (120°) condition is a classical ground state for $J_z \geq -1/2$ and $J_z < 1$ for the classical XXZ Hamiltonian (There is an additional classical phase transition at the Heisenberg point $J_z = 1$, which we do not explore). For the quantum case, *only* at the $J_z = -1/2$ point, there is a direct one to one correspondence between the classical and quantum ground states, i.e. any valid three-coloring can be interpreted as both a classical ground state spin configuration and a quantum ground state spin-$1/2$ wavefunction. However, there remains an important difference between the classical and quantum solutions even at this point - quantum mechanically, the Hamiltonian is block diagonal in definite total S_z due to the $U(1)$ symmetry, and thus the eigenfunctions in each of those sectors must have definite total S_z. Therefore, *projecting* each three-coloring solution to each total S_z sector must *also* be an exact ground state of that total S_z sector, thereby justifying the projection in Eq. (7). Conversely, this also implies that this exactly solvable point exists in all total S_z sectors.

The three-coloring wavefunctions when projected to the one particle sector (or one spin-down sector), can be viewed as the wavefunction of a single particle on the kagome lattice. One such example has been represented in Fig. 2. Depending on the color associated with the site, the amplitudes are 1, ω or ω^2. Taking linear combinations of single particle wavefunctions (i.e. adding their amplitudes site by site) is exactly equivalent to taking linear combinations of projected colorings, since $P_1|C_1\rangle - P_1|C_2\rangle = P_1(|C_1\rangle - |C_2\rangle)$. This

concept will be used in the next section when discussing resonating color loops.

The total number of three-coloring ground states scales exponentially with system size. However, there are two subtleties to be considered when counting the exact number of linearly independent solutions when projecting to definite S_z. First, when one interchanges colors (consistently for all sites), the new coloring $|C'\rangle$ is not linearly independent of the original one $|C\rangle$. This can be seen by redefining,

$$|\downarrow\rangle' \equiv \omega|\downarrow\rangle \tag{13}$$

which is equivalent to the transformation (from old to new variables)

$$\begin{aligned} r &\to g \\ b &\to r \\ g &\to b \end{aligned} \tag{14}$$

This is equivalent to a rotation of the spins in the xy plane by an angle of $2\pi/3$ around the z axis. Under this transformation each spin configuration (and hence the overall wavefunction) is only rescaled by a constant phase $\omega^{N_\downarrow}$ where $N_\downarrow$ is the number of down spins. A similar transformation holds for $|\downarrow\rangle' \equiv \omega^2|\downarrow\rangle$ which leads to $r \to b$, $b \to g$, $g \to r$. Thus, these three-colorings are not linearly independent and should not be counted more than once.

The second subtlety when counting the number of colorings is that not all colorings remain linearly independent when projected to definite total S_z. This is best exemplified by considering the case of the fully ferromagnetic sector. Here, even though the number of three-colorings is exponential, there is only one unique solution possible. Thus, to determine the precise number of linearly independent many body states, we evaluate the rank ($R(S)$) of the overlap matrix $\mathbf{S}_{CC'} = \langle C|C'\rangle$. The matrix elements are calculated efficiently and the matrix numerically diagonalized for this purpose. (Details of the calculation of the matrix elements in this non-orthogonal basis have been discussed at length in the supplemental information of Ref.[17] and are hence not presented here.) This enumeration of three-coloring states and their counting is an essential part of the diagonalizations we perform in the restricted subspace of the full Hilbert space.

Till this stage, our discussion has focused on the $J_z = -1/2$ point, which is only one point in the parameter space of the XXZ model. However, as mentioned in the introduction, the concept of color degrees of freedom and three-coloring states is useful more generally; we will show this more explicitly in the subsequent sections. For example, in an attempt to minimize both parts of Eq. (4), we have diagonalized the XXZ Hamiltonian in the three-coloring basis numerically by solving the generalized eigenproblem,

$$\mathbf{Hx} = E\mathbf{Sx} \tag{15}$$

where $\mathbf{H}_{CC'} = \langle C|H|C'\rangle$, E is the eigenenergy and $\mathbf{x}$ is the eigenvector of coefficients of three-color basis states.

The results of the ground state energy in the three-color basis are compared to the exact ground state energy in the full (Ising) basis for some representative examples in Fig. 3. The three-coloring states do not form a complete set in a specified S_z sector and hence are incapable of describing arbitrary wavefunctions. However, for two of the three examples shown, we *do* obtain the *exact* energy for $J_z \geq -1/2$. For these, the exact wavefunctions do lie completely in the three-coloring manifold with a total ground state energy equal to $E_{XXZ0} + (J_z + 1/2)\left(\frac{N}{2} - 2\sum_i n_i\right)$ for a N site kagome lattice. These numerical findings suggest the existence of an analytic way of understanding the three-coloring superposition and we will develop the appropriate concepts for proving that this is indeed the case.

A third example ($36d$ cluster at $2/3$ magnetization or $1/6$ filling), where the existence of a chiral spin liquid was argued previously[34], is also shown in the central panel of Fig. 3. While we do not obtain the exact energy for $J_z \geq -1/2$ for this case, the general trends appear consistent with exact diagonalization, suggesting that the three-coloring basis may be capable of representing certain chiral spin liquids. In this paper we will focus on the cases where the three-coloring basis is an exact representation of the kagome ground state in high magnetization (low filling) sectors.

III. RESONATING COLOR LOOPS

In this section we will develop the machinery to generate, on some lattices and at low density, simultaneous ground states of H_{XXZ0} and H_{zz} making them frustration free ground states of $H_{XXZ0} + (J_z + \frac{1}{2})H_{zz}$. Unfortunately, no single three-coloring is such a ground state, except in the extreme case of a fully polarized state. Instead, we need to construct linear combinations of three-colorings; such states are already ground states of H_{XXZ0} and so our focus will be developing linear combinations which minimize H_{zz} at low density.

The key tool in accomplishing this task will be resonating color loops (RCL). A RCL is generated by taking a single closed "two-color" loop (comprising, say of green and blue colors) and replacing it with a linear combination of the two different green-blue colorings over that loop with a relative minus sign between them. For example, consider the closed loop corresponding to the hexagonal plaquette on the kagome lattice. Then, the quantum state

$$|\text{RCL}\rangle = |gbgbgb\rangle - |bgbgbg\rangle \tag{16}$$

is what we define as a green-blue RCL (see Fig. 4). For the purpose of this work, the definition of the RCL adopted is always of the form Eq. (16). However, in principle, it is possible to generalize the concept of RCL to other linear superpositions, with certain desirable properties. The local resonating structure of RCLs is thus reminiscent of resonating valence bond (RVB) states.

Consider a fixed three-coloring with some number of two-color loops which are adjacent only to a third color, i.e. an *isolated* two-color loop (ICL). Any k ICL can be replaced with k RCL and the resulting state will be a linear superposition of 2^k three-colorings. This follows because if an entire two-colored

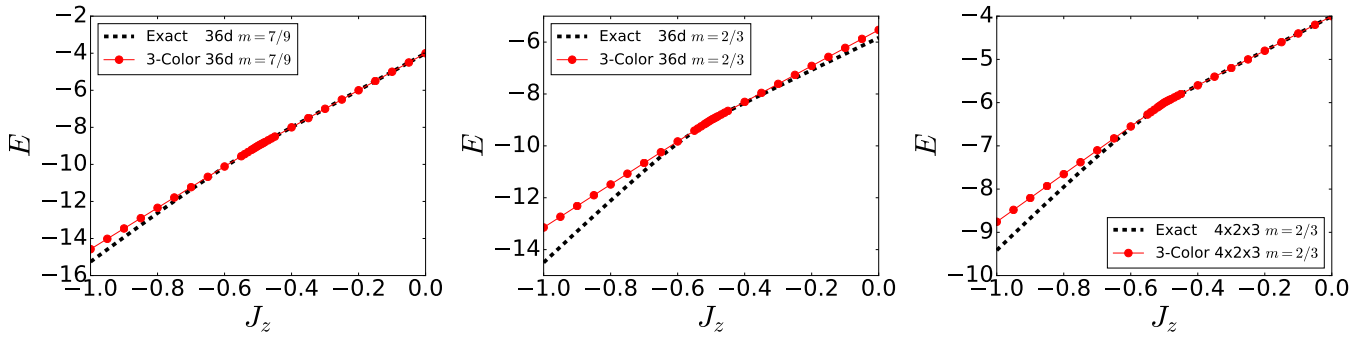

Figure 3. Comparison of ground state energies from exact diagonalization and diagonalization in the three-color basis as a function of J_z (in units of $J = 1$) for the (left panel) 36d cluster for $S_z = 14$ ($m = 7/9$ or 1/9 filling of bosons) and (central panel) for $S_z = 12$ ($m = 2/3$ or 1/6 filling of bosons) in the range $-1 \leq J_z \leq 0$. For a thin torus such as the $4 \times 2 \times 3$ torus for $S_z = 8$ ($m = 2/3$ or 1/6 filling of bosons) shown in the rightmost panel, the exact solution holds. In cases where the Hamiltonian is frustration free for $J_z \geq -1/2$, (here, leftmost and rightmost panels) the exact ground state solution holds for arbitrary $J_z \geq -1/2$.

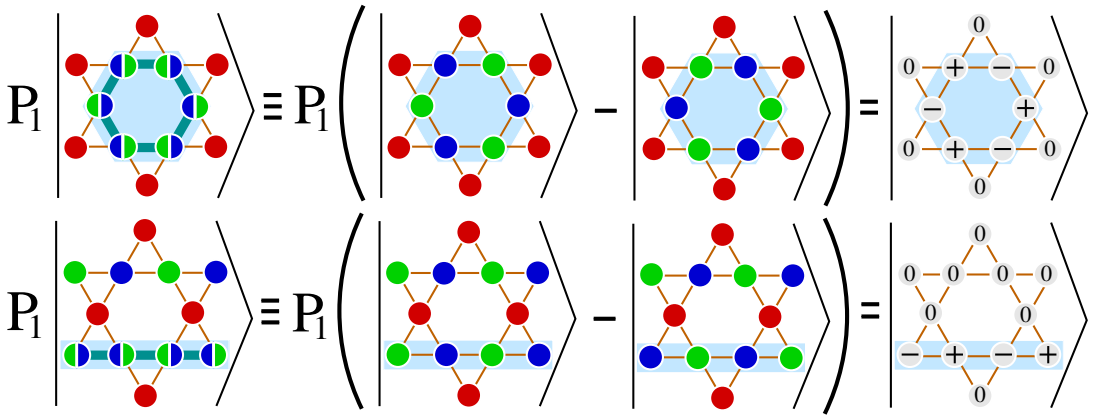

Figure 4. (Color online) Definition of resonating color loops on a kagome lattice. Each RCL is obtained by taking a difference of two three-colorings, which differ only on a single two-color loop. In the top panel, the RCL is located on a hexagon and in the bottom panel it is located on a topological (non-contractible) loop, here winding along the x direction. The RCLs when projected to a single spin-down (magnon) sector are exactly equal to localized or topological magnons on the kagome lattice up to a (projective) phase, and an innocuous normalization.

loop (say of green and blue) is surrounded by red, then swapping green and blue within that loop still leaves no edge with the same color on both vertices. As an example, consider the $\sqrt{3} \times \sqrt{3}$ coloring of the kagome lattice (Fig. 1). This coloring has isolated two-color hexagonal loops. We can take any number of these hexagons and turn them into RCLs. Alternatively, on the $q = 0$ coloring on the kagome lattice (Fig. 1) there are isolated non-contractible loops which can be turned into a RCL. It is interesting to note that on a coordination-4 lattice of triangles every site is part of an isolated two-color loop.

Now that we have a linear combination of three-colorings generated by replacing ICL with RCL, we can consider the role of projection on these states. In particular, we will see that if we globally project a state with k RCL into the sector of k spin-down (i.e. P_k), then there will be *exactly one* spin-down constrained to each RCL and *no* spin-down outside the RCL. A $k = 2$ representative example is shown in Fig. 5.

To see this why this particle localization happens, we first note that the difference of two colorings is destroyed by projecting into the fully spin-up (no boson) sectors on a given RCL, i.e.

$$P_0^{\text{RCL}} \left(|C_m^1\rangle - |C_m^2\rangle \right) = 0 \tag{17}$$

where C_m^1 and C_m^2 are arbitrary colorings on the motif denoted by m. It then follows that $P_0|\text{RCL}\rangle = 0$ (here it is important the RCL is the difference of two loops). Now, let us consider, as an example, P_2 applied to a quantum state with 2 RCL and decompose P_2 into the sum of tensor products of projectors over the two RCLs and the rest of the system respectively, written explicitly as

$$\begin{aligned} P_2 =& P_2^{\text{RCL}_1} \otimes P_0^{\text{RCL}_2} \otimes P_0^{\text{rest}} + \\ & P_0^{\text{RCL}_1} \otimes P_2^{\text{RCL}_2} \otimes P_0^{\text{rest}} + \\ & P_0^{\text{RCL}_1} \otimes P_0^{\text{RCL}_2} \otimes P_2^{\text{rest}} + \\ & P_1^{\text{RCL}_1} \otimes P_1^{\text{RCL}_2} \otimes P_0^{\text{rest}} + \\ & P_1^{\text{RCL}_1} \otimes P_0^{\text{RCL}_2} \otimes P_1^{\text{rest}} + \\ & P_0^{\text{RCL}_1} \otimes P_1^{\text{RCL}_2} \otimes P_1^{\text{rest}} \\ \implies P_2 =& P_1^{\text{RCL}_1} \otimes P_1^{\text{RCL}_2} \otimes P_0^{\text{rest}} \end{aligned} \tag{18}$$

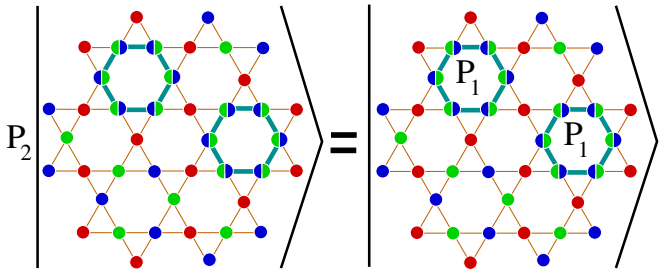

Figure 5. (Color online) A representative example of projection on to the $k = 2$ spin-down sector on a configuration with two RCLs. The projection properties of RCLs ensure localization of bosons/spin downs to localized hexagons.

The last equality follows from Eq. (17), as any term in the sum with P_0^{RCL} on an RCL is destroyed. This is schematically shown in Fig. 5. The above generalizes straightforwardly to k RCLs projected to k spin-down sector. Using this machinery, we thus have an ability to localize down-spins onto any ICL. This ability will allow us to minimize H_{zz} by ensuring that two spin-downs are never nearest neighbors.

In the next two sections we will see (1) that this argument (RCL when projected into a single spin-down) is essentially a quantum coloring language to describe kagome flatband magnons and (2) that on a variety of coordination-4 lattice of triangles such as the kagome lattice, the kagome ladder and the squagome lattice, at high magnetizations (i.e. at low fillings), the many body ground state is a tensor product of RCLs projected to that S_z sector.

IV. KAGOME FLAT BAND MODES FROM RESONATING COLOR LOOPS

In the previous section we considered how an RCL can be used to localize down spins on certain motifs. In this section we are going to consider systems with a single RCL being projected into the single spin-down sector (i.e. P_1) finding an exact correspondence between these projected RCLs and the localized and topological magnons[35] associated with the flatband of the kagome lattice. To understand this result, we first review the results of Ref.[36] which explained the existence of kagome lattice flat band modes using a localized basis of single-particle orbitals.

First we note that the XXZ Hamiltonian with a single down spin corresponds to the non-interacting tight binding model on the kagome lattice giving three bands with dispersions,

$$\epsilon_0(\mathbf{q}) = -t \tag{19a}$$

$$\epsilon_\pm(\mathbf{q}) = \frac{t}{2}\Big(1 \pm \sqrt{3 + 2\Lambda(\mathbf{q})}\Big) \tag{19b}$$

where $\Lambda(\mathbf{q}) = \mathbf{cos}(\mathbf{q}\cdot\mathbf{a_1}) + \mathbf{cos}(\mathbf{q}\cdot\mathbf{a_2}) + \mathbf{cos}(\mathbf{q}\cdot\mathbf{a_3})$. For $t > 0$, the flat band becomes the lowest energy band and at $\mathbf{q} = 0$, ϵ_- touches the flat band. Thus, on a kagome lattice on a finite torus (periodic boundary conditions), with N unit cells with a finite momentum grid with N points, there are $N + 1$ single particle states at $\epsilon = -t$.

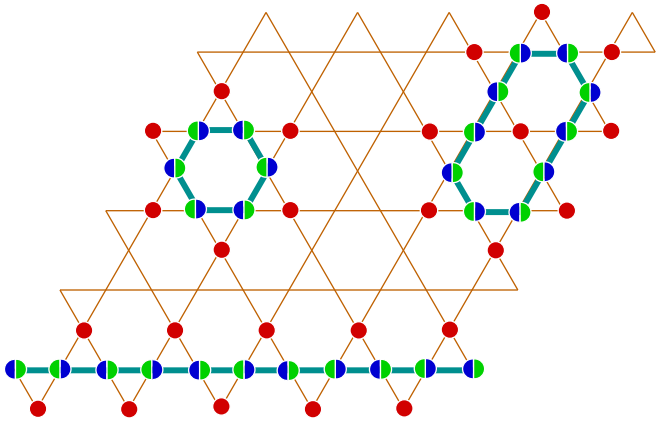

Figure 6. (Color online) Representative locations of localized and topological single particle modes as resonating color loops are shown, including a 10 site loop that may be thought of as a composition of two hexagonal localized modes. Fig. 4 shows how to transcribe the above RCL representation into the magnon modes. Apart from the *single* RCL at a chosen representative location, the rest of lattice is the same valid three-coloring, which makes the cancelation at all other sites exact.

The flatness of the band allows us to take linear combinations of single particle states freely while remaining eigenstates. This leads to a useful and insightful representation that results in localized eigenstates[36], given by,

$$A_R{}^\dagger = \frac{1}{\sqrt{L}}\sum_{j=1}^{L}(-1)^j b_j^\dagger \tag{20}$$

where L is the length of any contractible loop of length $4m+2$ or non contractible loop of length $2m$ where m is an integer and j refers to the index of lattice sites numbered in a contiguous order. When $L = 6$, this mode is localized on a hexagonal motif, and is represented in the right most side of the top panel of Fig. 4 ignoring the normalization of $\sqrt{6}$. Intuitively, this mode can be understood using a simple quantum interference argument. The topology of the kagome is such that the "+" and "−" contributions from hopping on to the vertices pointing away from the hexagon cancel out destructively and thus such a localized state becomes an exact ground state of the tight binding Hamiltonian.

We now identify the relation between the quantum coloring language and these localized single particle orbitals. By taking a single projected RCL on a hexagon shown in Fig. 4 a pattern of alternating $(\omega - \omega^2)$ and $(\omega^2 - \omega)$ is obtained on the hexagon with 0 everywhere else. Up to an overall phase factor, the mode is identical to the alternating pattern of $+$ and $-$ described above. In fact, this argument holds for arbitrary $L = 4m + 2$, such as the 10 site loop (which can be alternately viewed as a superposition of two localized single-particle hexagon wavefunctions) which corresponds to a projected 10 site RCL (see Fig. 6). Thus projected RCLs have the form as in Eq. (20).

The set of N hexagon single particle modes is not completely linearly independent; the wavefunction of the N^{th} hexagonal mode can be rewritten as a linear combination of

the remaining $N-1$ modes[36]. Since the expected count of the lowest degenerate states is $N+1$, this leaves us with two modes to be determined. Ref.[36] showed that these correspond to two topological modes, coming from any choice of two non-contractible loops along the two periodic directions on the torus. An example of such a loop in the horizontal direction is shown in Fig. 6 (bottom). Once again, this topological magnon has a natural meaning in the basis of three colors, and as is shown in Fig. 4, it is identical to an RCL defined on a two-color loop along the horizontal direction.

We have thus shown that every single particle magnon corresponding to the kagome flat band is exactly an RCL of a certain type. This is particularly useful, because it allows us to freely swap concepts between two distinct languages. In particular, in the next section we will provide a new interpretation of many-body wavefunctions constructed at low magnon fillings, in terms of RCLs.

V. LOW DENSITY EXACT SOLUTIONS FROM RESONATING COLOR LOOPS

Now that we have developed the connection between RCLs and localized and topological magnons, we will explicitly construct many-body solutions which minimize both H_{XXZ0} and H_{zz}, for certain cases of net magnetization. We begin with the case of a narrow kagome torus with dimensions $L_x \times (L_y = 2) \times 3$. For $L_x = 4$, we show in Fig. 7 (top panel) that the RCLs are "stripes" (blue-green local motifs) on which the closely-packed localized magnons reside. Since each RCL is associated with a winding loop of 4 sites (along with 2 other padded sites) and each such motif contributes a single magnon or hard-core boson, the filling is exactly $1/6$. At this filling, denoted by f, the exact many body wavefunction is therefore a product state on these local motifs,

$$|\psi\rangle = P_{Nf}\Big(\prod_{m=\text{motif}} |\text{RCL}_m\rangle \otimes \prod_{o=\text{other}} |r_o\rangle\Big) \qquad (21)$$

Since the magnons are never located on neighboring sites, due to the zero amplitude red sites (as indicated in the Fig. 7) they completely avoid nearest neighbor density-density interactions (See Eq. (6)) thereby minimizing H_{zz}. Thus, this wavefunction is the exact ground state for arbitrary repulsive interactions ($J_z \geq 0$). This closely-packed construction has been noted earlier in the literature in the " $+/-$ " magnon language[35,37–41]. However, since the wavefunction is also a product of RCLs, the wavefunction has an exact representation in a basis of valid three-colorings, it also becomes the ground state for any $J_z \geq -1/2$, *starting now* from Eq. (4) via its hard-core boson counterpart. The RCL is thus able to localize down spins (or particles) on motifs (eg. local hexagons or topological loops) and keeps them apart.

This idea of constructing single magnon wavefunctions and the extension to many body wavefunction generally applies to many other lattices, fillings and tilings (choices of motifs). For example, for $1/9$ filling, the idea generalizes to the infinite kagome and on any finite cluster that accommodates the $\sqrt{3} \times \sqrt{3}$ pattern. This includes the $36d$ cluster and certain quasi one-dimensional cylinders[42]. Each magnon is now confined to a local hexagon and using the formalism of projected RCLs, the many body wavefunction is simply a product state of RCLs and color red (a) on sites that do not belong to the hexagonal RCLs. Since the tiling of RCLs can be done in three distinct ways (due to the three-fold symmetry of the $\sqrt{3} \times \sqrt{3}$ pattern), our construction yields a three-fold degenerate ground state solution.

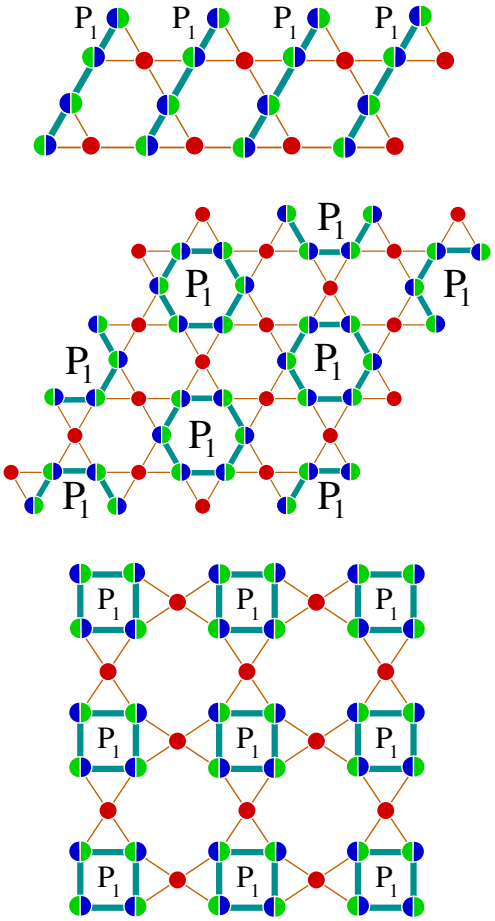

Figure 7. (Color online) Many-body ground state wavefunction for magnons represented in a three-coloring basis. The top panel shows the case of 4 magnons (bosons) on the $4 \times 2 \times 3$ torus. The construction generalizes to L magnons on the $L \times 2 \times 3$ lattice i.e. 1/6 filling. Each magnon is confined to a strip and the many-body wavefunction is simply a product state of corresponding RCLs. Similar constructions apply at 1/9 filling to the infinite kagome and any finite cluster that accommodates the $\sqrt{3} \times \sqrt{3}$ pattern (middle panel). For 1/6 filling the construction also generalizes to two dimensions on the "squagome" lattice built up of triangular motifs (lowest panel).

For $1/6$ filling, we may extend the above exact solutions to the two-dimensional "squagome" lattice, now using the motifs shown in Fig. 7 (bottom panel). Each motif is once again associated with an RCL, and because of the S_z or number projection operation, the intermediate sites between the magnons have zero amplitudes, with the magnon or boson residing on the square plaquettes.

This analysis also immediately gives the ground state in the

coloring basis for any lower density. If a wavefunction with k RCLs is the ground state of Eq. (4), then the wavefunction obtained by replacing any subset of the k RCLs by ICLs is still a ground state. In the thermodynamic limit, these fill in all lower densities. In particular, this means that these phases extend to the quantum critical point at $J_z = -1/2$ on the kagome for all filling $\leq 1/9$.

Thus, we have shown that several low magnon (particle) density/high magnetization solutions can be exactly constructed from three-coloring states. In each individual example presented, the wavefunction constructed minimizes both H_{XXZ0} and H_{zz}, and hence is the *exact* ground state wavefunction for any $J_z \geq -1/2$. Said differently, the magnons confined to their individual motifs (strip, hexagon etc.) completely avoid repulsion ($J_z > 0$) at low density and minimize their kinetic energy by staying localized. However the color-magnon transformation shows that even under attractive interactions, the localized magnons do not immediately condense - rather there is a *critical attraction* strength ($J_z = -1/2$) which is needed for this to happen. While this result is true and mathematically rigorous only at low density, where the magnons form a crystal[40], a natural question that arises is whether the coloring manifold is responsible for the origin of the spin liquid ground state, expected at one-sixth (2/3 magnetization)[34,43] and half filling (zero magnetization).

VI. DMRG FOR H_{XXZ} FOR THE ZERO MAGNETIZATION SECTOR

In lieu of such an understanding, we now turn our attention to a numerical study in the case of half filling ($S_z = 0$) where the ground state does not have an exact three-coloring representation. A previous DMRG study[44] argued that the spin liquid at the Heisenberg point ($J_z = 1$) adiabatically continues both to the XY ($J_z = 0$) and Ising ($J_z \gg 1$) limits. Also, previous ED studies on 36 and 48 site clusters showed remarkable similarities in the low energy spectrum from $J_z = 0$ to $J_z = 1$[45] and the Ising limit[46]. In addition, another ED study on 36 sites strongly suggested adiabatic continuity for all $J_z \gtrsim -0.4$ (and possibly up to $XXZ0$)[17]. Here, we extend these results by performing large-scale DMRG calculations (using ITensor[47]); these results support the finding that the spin liquid phase extends to the $J_z = -1/2$ point[17,48].

We study the zero-magnetization ground states in a wide range of J_z, from $J_z = 5$ to $J_z = -1$. To better focus on the $J_z = -1/2$ point, we have shown the results only up to $J_z = 1$; the ground state changes smoothly with no signs of a phase transition between $J_z = 1$ and $J_z = 5$. We focus on the $XC8$ cylindrical geometry (which is depicted in Fig. 10) and keep the bond dimension (number of states in DMRG) up to 7000. The total energy has been extrapolated to infinite-length; our extrapolated results are shown in Fig. 8 as a function of J_z. Details of the extrapolation are given in Appendix A.

For the region of $J_z < -1/2$ the ground state is ferromagnetic (albeit phase-separated due to the total $S_z = 0$ constraint), and thus the ground state energy for this region equals $J_z/2$, as indicated by the good agreement between our DMRG

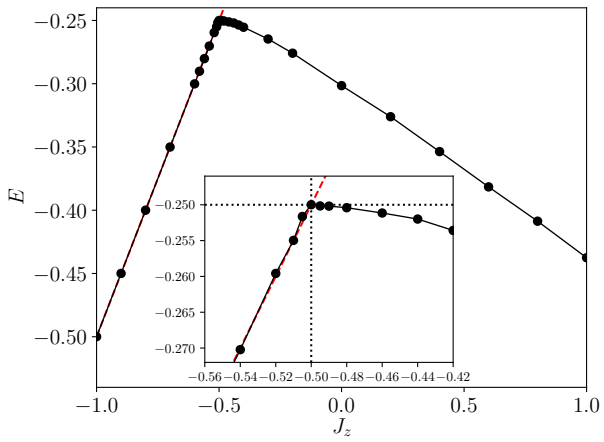

Figure 8. (Color online) Ground state energy per site from DMRG for the XC-8 cylinder in the limit of infinite length for the range $-1 \leq J_z \leq 1$. The red dashed line indicates the energy ($= J_z/2$) of pure ferromagnetic states. The inset zooms into a narrow range around $J_z = -1/2$. The errorbars are presented but smaller than the symbol sizes. The dotted lines in the inset indicate the exact energy $-1/4$ at $J_z = -1/2$.

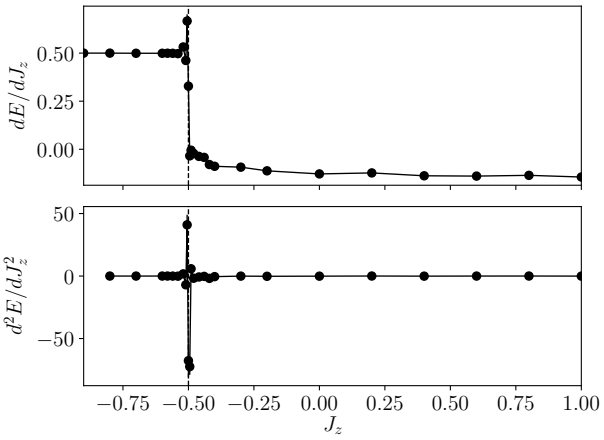

Figure 9. First and second derivative of the energy per site as a function of J_z. The errorbars are presented but smaller than the symbol sizes. The discontinuity in the first derivative and the peak in the second derivative at $J_z = -1/2$ signal the occurrence of a quantum phase transition.

data points and the red dashed line. On going from $J_z = 1$ to $J_z = 0$ the energy increases monotonically and smoothly, indicating an absence of a phase transition in this region, consistent with Ref.[44]. Importantly, this smooth monotonic behavior continues across $J_z = 0$ and a kink is seen only at (or close to) $J_z = -1/2$, strongly suggesting that the exactly solvable point is a transition point between spin liquid and ferromagnetic states. Evidence for such a transition is further clarified by monitoring the first and second derivatives of energy, shown in Fig. 9; the first derivative has a discontinuity and the second derivative has a peak at $J_z = -1/2$.

In practice, the DMRG simulations were found to get stuck in valence bond solid states or metastable states with edge

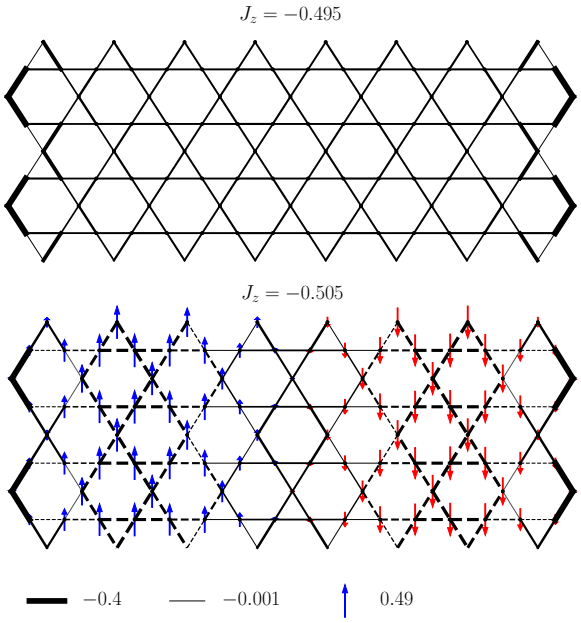

Figure 10. (Color online) Spatial profile of spin moments $\langle S_i^z \rangle$ and valence bond energies $\langle \mathbf{S}_i \cdot \mathbf{S}_j \rangle$ on a representative XC-8 cylinder for $J_z = -0.495$ and $J_z = -0.505$. The maximum spin moment for $J_z = -0.495$ is $\sim 5 \times 10^{-4}$. The solid (dashed) bonds represent the negative (positive) valence bond energies.

spins. We thus had to run different random initial states to converge to the lowest energy spin liquid state. This is, in principle, consistent with a scenario that the XXZ model is associated with a line of critical points[17] and that the choice of geometry typically picks one state over the other. One concrete example of this observation is discussed in Appendix B at $J_z = -0.35$ where the energy per site of the competing VBS and spin liquid differ only by $\approx 10^{-4}$. In general, we found that the convergence is particularly difficult around $J_z = -0.4$, which may suggest the need for further detailed future studies in this region with larger systems and different geometries.

For $J_z < -1/2$ we started our DMRG calculations with two ferromagnetic domains. Not doing so led to more ferromagnetic domains with slightly higher energy than the two domain solution. Magnetic pinning field is also applied to further stabilize the states in the region $-0.52 \leq J_z < -0.5$ close to the transition point. Further details are discussed in Appendix A.

Fig. 10 shows local spin and valence bond order parameters at two representative points $J_z = -0.495$ and $J_z = -0.505$ very close to the transition point. Clearly, for $J_z = -0.495$ there is no local order (for the order parameters measured) and for $J_z = -0.505$ a ferromagnetic state is stabilized; domains are observed as the system prefers to phase-separate to maintain the total $S_z = 0$ constraint.

VII. CONCLUSION

In summary, we have explored properties of quantum three-coloring states and developed an exact one-to-one correspondence between quantum three-colors and the localized and topological magnons that make up the flat band modes on the kagome lattice. While both perspectives and concepts have existed in the literature in various forms (classical three-colorings, quantum magnons), our work makes their connection concrete for the quantum case and generalizes it to both the single and multi magnon case. It is no coincidence that the two color loops in a three-coloring state, and the magnon modes in the kagome flat band have geometrical similarities; our work shows why this is the case.

Extending this connection, we have expressed exact many-body ground state wavefunctions for special high magnetizations (or low fillings in the bosonic language) in a three coloring basis; this proves their validity for all $J_z \geq -1/2$ showing the equivalence of the XY and Ising regimes, for these magnetization sectors. Using the color-magnon transformation, our results extend the range of validity of exact solutions which have been argued to hold for $J_z \geq 0$ (repulsive case in the boson language), to $-1/2 \leq J_z \leq 0$ (*attractive* case). We have also highlighted the important role and subtleties of number projection at low fillings. For the case of half filling/zero magnetization, our numerical DMRG calculations suggest that the physics of the Heisenberg point is crucially connected to the $J_z = -1/2$ point.

Finally, we note that in the present work, we have only considered the cases where a macroscopic superposition of three colorings describes product states in the magnon basis (these are incidentally also a subset of correlator product states[49]). However, it is natural to ask whether and/or how can one map a highly entangled state from the Ising or magnon basis to the three-color basis. In addition, the three-colorings present an attractive possibility of explaining the large number (exponentially scaling with system size) of singlets seen in the low energy spectrum in exact diagonalizations[50,51]. We hope to address these and related questions in the future.

VIII. ACKNOWLEDGEMENTS

HJC and BKC thank E. Fradkin, D. Kochkov and K. Kumar for an earlier collaboration. We thank O. Vafek, S. Sachdev, O.Tchernyshyov, P. Nikolic, V. Dobrosavljevic, F. Verstraete, A. Ralko, Y-C.He and M. Lawler for their encouragement and for useful discussions. This work was supported through the Institute for Quantum Matter at Johns Hopkins University, by the U.S. Department of Energy, Division of Basic Energy Sciences, Grant DE-FG02-08ER46544. HJC acknowledges start up funds at Florida State University. SP acknowledges the support (17IRCCSG011) of IRCC, IIT Bombay. We gratefully acknowledge the Johns Hopkins Homewood High Performance Cluster (HHPC) and the Maryland Advanced Research Computing Center (MARCC), funded by the State of Maryland, for computing resources. This research is also part of the BlueWaters sustained petascale computing

project, which is supported by the National Science Foundation (award numbers OCI-0725070 and ACI-1238993) and the State of Illinois. The DMRG calculations were performed using the ITensor C++ library (version 2.1.1), https://itensor.org/

[1] M. P. Shores, E. A. Nytko, B. M. Bartlett, and D. G. Nocera, Journal of the American Chemical Society **127**, 13462 (2005), pMID: 16190686, https://doi.org/10.1021/ja053891p.
[2] J. S. Helton, K. Matan, M. P. Shores, E. A. Nytko, B. M. Bartlett, Y. Yoshida, Y. Takano, A. Suslov, Y. Qiu, J.-H. Chung, D. G. Nocera, and Y. S. Lee, Phys. Rev. Lett. **98**, 107204 (2007).
[3] P. Mendels and F. Bert, Comptes Rendus Physique **17**, 455 (2016).
[4] H. O. Jeschke, F. Salvat-Pujol, and R. Valenti, Phys. Rev. B **88**, 075106 (2013).
[5] C. Zeng and V. Elser, Phys. Rev. B **42**, 8436 (1990).
[6] Y. Ran, M. Hermele, P. A. Lee, and X.-G. Wen, Phys. Rev. Lett. **98**, 117205 (2007).
[7] S. Yan, D. A. Huse, and S. R. White, Science **332**, 1173 (2011).
[8] S. Depenbrock, I. P. McCulloch, and U. Schollwöck, Phys. Rev. Lett. **109**, 067201 (2012).
[9] Y. Iqbal, F. Becca, S. Sorella, and D. Poilblanc, Phys. Rev. B **87**, 060405 (2013).
[10] H.-C. Jiang, Z. Wang, and L. Balents, Nat. Phys. **8**, 902 (2012).
[11] T. Tay and O. I. Motrunich, Phys. Rev. B **84**, 020404 (2011).
[12] Y.-C. He, M. P. Zaletel, M. Oshikawa, and F. Pollmann, Phys. Rev. X **7**, 031020 (2017).
[13] H. J. Liao, Z. Y. Xie, J. Chen, Z. Y. Liu, H. D. Xie, R. Z. Huang, B. Normand, and T. Xiang, Phys. Rev. Lett. **118**, 137202 (2017).
[14] L. Messio, B. Bernu, and C. Lhuillier, Phys. Rev. Lett. **108**, 207204 (2012).
[15] Z. Hao and O. Tchernyshyov, Phys. Rev. Lett. **103**, 187203 (2009).
[16] A. Ralko, F. Mila, and I. Rousochatzakis, Phys. Rev. B **97**, 104401 (2018).
[17] H. J. Changlani, D. Kochkov, K. Kumar, B. K. Clark, and E. Fradkin, Phys. Rev. Lett. **120**, 117202 (2018).
[18] T. Li, ArXiv e-prints (2011), arXiv:1106.6134 [cond-mat.str-el].
[19] K. Essafi, O. Benton, and L. D. C. Jaubert, Nat. Commun. **7**, 10297 (2016).
[20] P. W. Leung and V. Elser, Phys. Rev. B **47**, 5459 (1993).
[21] T. Momoi and M. Suzuki, Journal of the Physical Society of Japan **61**, 3732 (1992).
[22] A. B. Harris, C. Kallin, and A. J. Berlinsky, Phys. Rev. B **45**, 2899 (1992).
[23] C. L. Henley, Phys. Rev. B **80**, 180401 (2009).
[24] D. A. Huse and A. D. Rutenberg, Phys. Rev. B **45**, 7536 (1992).
[25] J. T. Chalker, P. C. W. Holdsworth, and E. F. Shender, Phys. Rev. Lett. **68**, 855 (1992).
[26] S. Sachdev, Phys. Rev. B **45**, 12377 (1992).
[27] J. von Delft and C. L. Henley, Phys. Rev. Lett. **69**, 3236 (1992).
[28] O. Cépas and A. Ralko, Phys. Rev. B **84**, 020413 (2011).
[29] C. Castelnovo, C. Chamon, C. Mudry, and P. Pujol, Phys. Rev. B **72**, 104405 (2005).
[30] J. M. Luttinger and L. Tisza, Phys. Rev. **70**, 954 (1946).
[31] V. Elser, Phys. Rev. Lett. **62**, 2405 (1989).
[32] J.-C. Domenge, P. Sindzingre, C. Lhuillier, and L. Pierre, Phys. Rev. B **72**, 024433 (2005).
[33] Z. Xiong and X.-G. Wen, ArXiv e-prints (2012), arXiv:1208.1512 [cond-mat.stat-mech].
[34] K. Kumar, H. J. Changlani, B. K. Clark, and E. Fradkin, Phys. Rev. B **94**, 134410 (2016).
[35] J. Schulenburg, A. Honecker, J. Schnack, J. Richter, and H.-J. Schmidt, Phys. Rev. Lett. **88**, 167207 (2002).
[36] D. L. Bergman, C. Wu, and L. Balents, Phys. Rev. B **78**, 125104 (2008).
[37] M. E. Zhitomirsky and H. Tsunetsugu, Phys. Rev. B **70**, 100403 (2004).
[38] J. Richter, J. Schulenburg, and A. Honecker, "Quantum magnetism in two dimensions: From semi-classical néel order to magnetic disorder," in *Quantum Magnetism*, edited by U. Schollwöck, J. Richter, D. J. J. Farnell, and R. F. Bishop (Springer Berlin Heidelberg, Berlin, Heidelberg, 2004) pp. 85–153.
[39] H.-J. Schmidt, Journal of Physics A: Mathematical and General **35**, 6545 (2002).
[40] S. Capponi, O. Derzhko, A. Honecker, A. M. Läuchli, and J. Richter, Phys. Rev. B **88**, 144416 (2013).
[41] S. D. Huber and E. Altman, Phys. Rev. B **82**, 184502 (2010).
[42] The $\sqrt{3}\times\sqrt{3}$ pattern can fit on cylinders of width that are multiples of 4 but not multiples of 6 by shifting ± 2 lattice constants in the periodic boundary condition along the cylinder circumference. These are $YC4+2$, $YC8-2$, $YC16-2$, $YC20+2$, etc. in the notation used in the DMRG literature. For cylinders of width that are multiples of 6, no such shifts are required.
[43] K. Kumar, K. Sun, and E. Fradkin, Phys. Rev. B **90**, 174409 (2014).
[44] Y.-C. He and Y. Chen, Phys. Rev. Lett. **114**, 037201 (2015).
[45] A. M. Läuchli and R. Moessner, ArXiv e-prints (2015), arXiv:1504.04380 [cond-mat.quant-gas].
[46] A. M. Läuchli, J. Sudan, and R. Moessner, ArXiv e-prints (2016), arXiv:1611.06990 [cond-mat.str-el].
[47] M. Stoudenmire and S.R. White, www.itensor.org.
[48] Here we do not address the scenario that the XXZ model for any $J_z \geq -1/2$ is part of a critical line as suggested in Ref.[17].
[49] H. J. Changlani, J. M. Kinder, C. J. Umrigar, and G. K.-L. Chan, Phys. Rev. B **80**, 245116 (2009).
[50] C. Waldtmann, H.-U. Everts, B. Bernu, C. Lhuillier, P. Sindzingre, P. Lecheminant, and L. Pierre, The European Physical Journal B - Condensed Matter and Complex Systems **2**, 501 (1998).
[51] F. Mila, Phys. Rev. Lett. **81**, 2356 (1998).
[52] J. P. F. LeBlanc, A. E. Antipov, F. Becca, I. W. Bulik, G. K.-L. Chan, C.-M. Chung, Y. Deng, M. Ferrero, T. M. Henderson, C. A. Jiménez-Hoyos, E. Kozik, X.-W. Liu, A. J. Millis, N. V. Prokof'ev, M. Qin, G. E. Scuseria, H. Shi, B. V. Svistunov, L. F. Tocchio, I. S. Tupitsyn, S. R. White, S. Zhang, B.-X. Zheng, Z. Zhu, and E. Gull (Simons Collaboration on the Many-Electron Problem), Phys. Rev. X **5**, 041041 (2015).

Appendix A: Energy extrapolation

In the main text, we showed results for the energy and certain observables from our DMRG calculations carried out in the zero magnetization ($S_z = 0$) sector. Here we describe further details of how the energy extrapolations to the infinite length limit were done using the finite size DMRG data. In Fig. 11 we show the energy extrapolations with the inverse length ($1/L_x$) on XC-8 cylinders for $J_z = -0.51, -0.505,$

and -0.495 close to the exactly solvable point $J_z = -1/2$. In our notation, the length is defined by the number of triangles along the longitudinal direction. We perform quadratic extrapolations for all J_z except $J_z = -0.505$, which does not show quadratic behavior but *does* show sufficiently small dependence on L_x. (We can thus estimate its $L_x \to \infty$ value accurately even without the extrapolation, as is shown in Fig. 11.)

For $J_z < -1/2$, where the ground states are ferromagnetic[17], we use ferromagnetic states with one domain wall as the starting states in our DMRG runs (the left half of the cylinder is initially fixed to a certain spin and the right half with the opposite spin type) as a way of avoiding getting stuck in the multiple domain wall states. We note that a state with any finite number of ferromagnetic domain walls in the thermodynamic limit will have zero energetic costs (per site) compared to the purely ferromagnetic or one-domain wall state.

We observe that in practice, for $J_z < -1/2$ and very close to $-1/2$, only long enough cylinders (≥ 8 in our cases) make the one-domain wall ferromagnetic states stable. The reason is as follows. Exactly at the transition ($J_z = -1/2$), the clean ferromagnetic state *without* a domain wall has the same energy as other (three coloring) ground states in the zero magnetization sector. The ferromagnetic state with a domain wall – whose existence is required to remain in the zero magnetization sector– raises the total energy at any finite size, and it is only for larger lattices that it is energetically favored. In a finite-size system, the domain-wall energy is not negligible, and DMRG ends up with non-ferromagnetic states for J_z very close to -0.5 (0.51 and 0.505 in this work).

Appendix B: Competitive energy candidates

In the main text we mentioned that we found a state with some strong discernible local bond energies, which we refer to as "VBS". (It must be noted that the pattern of bond energies is different from what is conventionally referred to as a VBS which has neighboring strong and weak bonds.) This VBS is strongly competitive with the spin liquid state in our DMRG calculations. Here we elaborate more on this finding.

Fig. 12 shows the bond expectation values of $\langle \bar{S}_i \cdot \bar{S}_j \rangle$ and on-site values of $\langle {S_i}^z \rangle$ for two different states obtained from two independent DMRG simulations for $J_z = -0.35$. The independent runs were started from two different random product states and the bond dimension was gradually increased during each sweep of the DMRG algorithm. The energy per site of the two states (when extrapolated to infinite bond dimension) differs only by 10^{-4} (the spin liquid has energy $-0.26329(2)$ per site while the VBS has energy $-0.263065(3)$ per site, see the top panel of Fig. 13), yet the states are visibly very different. This suggests (but does not rigorously prove) the possibility that the Hamiltonian is at a critical point in parameter space. Note that in Ref.[17], a critical line emanating from $J_z = -1/2$ at second nearest neighbor coupling $J_2 \approx 0$ has been reported based on diagonalization of the symmetric 36 site cluster.

To further analyze the proposal that the two states are separated by the $J_2 = 0$ line, we measure the "J_2 energy" defined as $\hat{H}(J_2) \equiv J \sum_{\langle\langle i,j \rangle\rangle} S_i^x S_j^x + S_i^y S_j^y + J_z \sum_{\langle\langle i,j \rangle\rangle} S_i^z S_j^z$, where $\langle\langle i,j \rangle\rangle$ denotes the next nearest neighbor sites. In Fig. 13 (left and center panels) we show the energies extrapolated with the truncation error in DMRG for both the energy and the "J_2 energy" per site. The J_2 energies for spin liquid and VBS are $0.0630(5)$ and $0.1061(15)$ respectively, which suggests that a small negative J_2 can drive the spin liquid to the VBS. The right panel in Fig. 13 shows explicitly this idea. We show the estimation energies with finite J_2, defined by $E(J_1, J_2) = E(J_1) + J_2 \langle H(J_2) \rangle$, for both the SL and the VBS. The crossing indicates the suggested transition between the SL and the VBS at small J_2.

We also mention that the errorbars in DMRG energies are defined by $1/5(E_{\text{variat}} - E_{\text{extrap}})$, where E_{variat} is the lowest variational energy and E_{extrap} is the extrapolated energy. Here the factor $1/5$ is chosen on the basis of experience and is typically used in the DMRG simulations[52]. The most conservative errorbars would be with the factor of 1, which then will cover the variational energy as an upper bound.

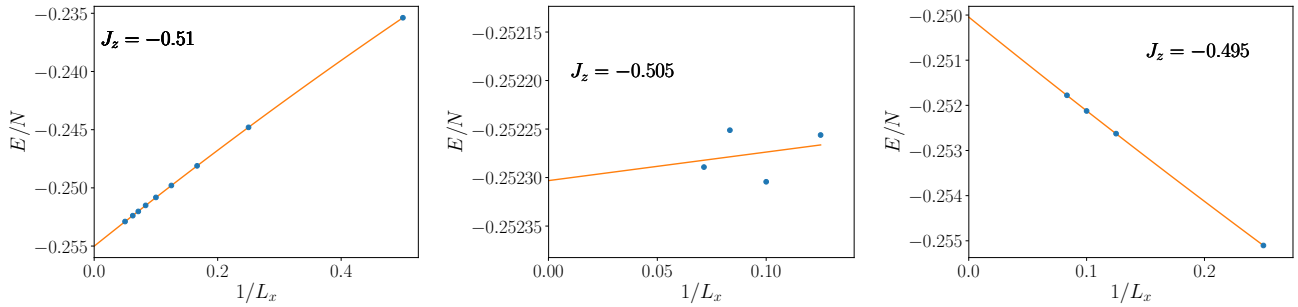

Figure 11. The extrapolations of the energies with $1/L_x$ for $J_z = -0.51$, -0.505, and -0.495 from the DMRG data. The lengths used for $J_z = -0.51$ are 10, 12, 14, 16, 18, 20, 22, 24, 26, 30, for $J_z = -0.505$ are 8, 10, 12, 14, and for $J_z = -0.495$ are 4, 8, 10, 12. The quadratic extrapolations are performed for $J_z = -0.51$ and -0.495, and the linear extrapolation is performed for $J_z = -0.505$. Notice the resolution of the y-axis tic marks for $J_z = -0.505$.

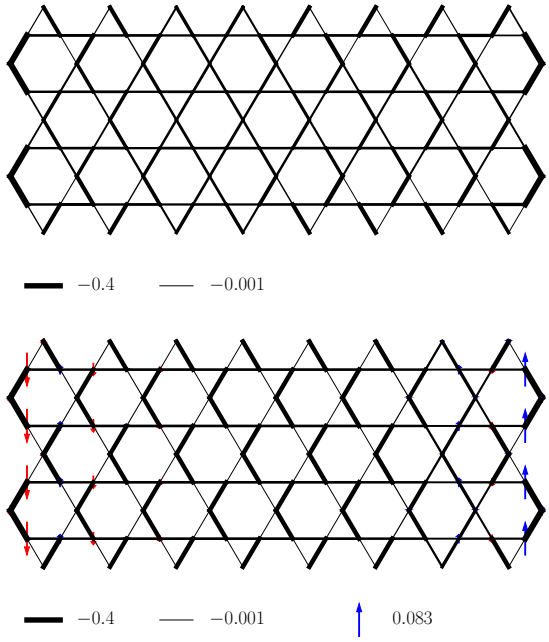

Figure 12. The spin liquid (upper panel) and the VBS (lower panel) states found in the DMRG simulations for $J_z = -0.35$. The widths of the bonds are proportional to the valence bond energies $\langle \vec{S}_i \cdot \vec{S}_j \rangle$, and the lengths of the arrows proportional to the spin moments $\langle S_i{}^z \rangle$. The maximum magnitude of the spin moment for spin liquid is $\approx 9 \times 10^{-6}$.

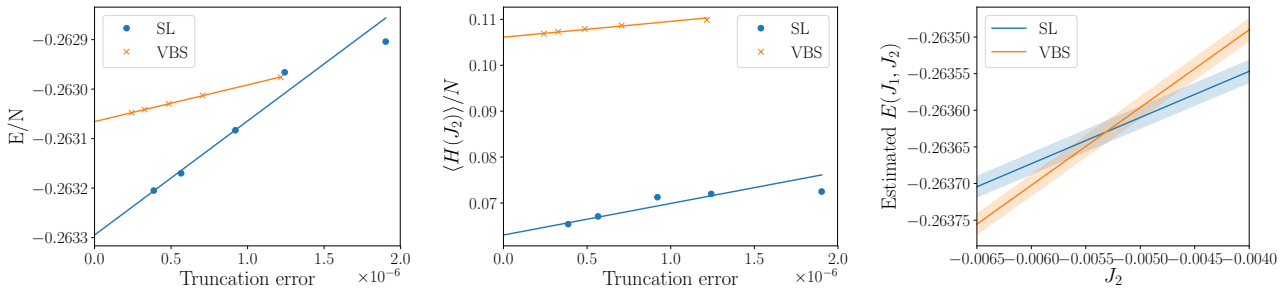

Figure 13. The extrapolation of the total energy (Left panel) and the "J_2 energy" (Center panel) per site with the truncation error in DMRG for the spin liquid (SL) and the VBS states as shown in Fig. 12. Right panel is the estimated energy with finite J_2, more explicitly $E(J_1, J_2) \equiv E(J_1) + J_2 \langle H(J_2) \rangle$. The crossing shows the suggested transition between SL and VBS with finite J_2. The light colors show the errorbars of $E(J_1, J_2)$.